

Article

Comparative Study on Vibration Characteristics of Biaxial Carbon/Glass Hybrid Wind Turbine Blades

Xin Jiang ^{1,*}, Yiming Jiang ¹, Ke Zhao ², Mingze Gao ², Jiayi Sun ¹, Lingfeng Fu ¹, Shidong Wen ¹ and Xiaoping Gao ² 

¹ School of Energy and Power Engineering, Inner Mongolia University of Technology, Hohhot 010051, China; 20211800252@imut.edu.cn (Y.J.); qq2093756632@163.com (J.S.); 20201800233@imut.edu.cn (L.F.); 20201800199@imut.edu.cn (S.W.)

² School of Science, Inner Mongolia University of Technology, Hohhot 010051, China; 20201000014@imut.edu.cn (K.Z.); 20221000003@imut.edu.cn (M.G.); gaexp@imut.edu.cn (X.G.)

* Correspondence: jiangxin@imut.edu.cn

Abstract: Endeavor to investigate the effect of carbon/glass hybrid ratio on blade flutter vibration characteristics. Based on the theory of strength of materials, the influence of carbon/glass hybrid ratio on the tensile strength of the sample under concentrated load was analyzed experimentally. The 10 KW wind turbine blade model was taken as the research object, and different carbon/glass hybrid ratios (2:6, 4:4, and 6:2) were selected as the blade reinforcement materials. The blade vibration characteristics were analyzed from three aspects: deformation displacement, blade mode, and stress distribution. The results showed that the blade hybrid ratio was between 6:2 and 4:4, and the maximum improvement in tensile performance was achieved. The hybrid ratios of 4:4 and 6:2 significantly improved the deformation resistance of the blades and required a shorter time to reach equilibrium. The blade stress was mainly concentrated at 1/3 of the blade, which was one of the main reasons for the phenomenon of blade waving.

Keywords: carbon/glass hybrid; tensile properties; vibration characteristics; deformation displacement; stress distribution



Citation: Jiang, X.; Jiang, Y.; Zhao, K.; Gao, M.; Sun, J.; Fu, L.; Wen, S.; Gao, X. Comparative Study on Vibration Characteristics of Biaxial Carbon/Glass Hybrid Wind Turbine Blades. *Appl. Sci.* **2023**, *13*, 9846. <https://doi.org/10.3390/app13179846>

Academic Editors: Angelo Luongo and Simona Di Nino

Received: 10 July 2023

Revised: 22 August 2023

Accepted: 26 August 2023

Published: 31 August 2023



Copyright: © 2023 by the authors. Licensee MDPI, Basel, Switzerland. This article is an open access article distributed under the terms and conditions of the Creative Commons Attribution (CC BY) license (<https://creativecommons.org/licenses/by/4.0/>).

1. Introduction

The vibration forms of wind turbine blades are mainly divided into swing, oscillation, and torsion. Vibration refers to the deformation or movement of blades under the action of the flow field, which in turn affects the flow field in the opposite direction, resulting in changes in the load size and distribution position of wind turbine blades [1,2]. Strong vibration of blades is often the root cause of accidents. When the pulse frequency approaches the natural vibration frequency of the blades resonance occurs, leading to cracks in the wind turbine blades and the occurrence of accidents [3]. Therefore, improving the vibration resistance performance of wind turbine blades is of great significance for improving the safety and reliability of blade materials for wind turbine operation [4].

Carbon/glass hybrid fiber material, as one of the new materials, has a lower cost compared to carbon fiber and can exhibit significant hybrid effects, resulting in better comprehensive benefits [5]. Gao et al. [6,7] studied the tensile properties of biaxial warp knitted and three-dimensional woven composites, and the results showed that the tensile strength of biaxial warp knitted composites in a certain direction is slightly higher than that of three-dimensional woven composites. Gao D et al. [8] prepared material samples by changing the volume ratio of carbon to glass, and conducted tensile and compressive tests. The results showed that the compressive strength of carbon fiber/glass HFRP specimens was on average higher than that of specimens with dispersed glass fiber distribution. Zeng et al. [9] selected a sample with a carbon glass volume ratio of 1:1 and conducted three different layers. The experiment showed that the 0° fully aligned structure with

relatively concentrated carbon fibers had the best tensile properties. In addition, numerous researchers have conducted research on the carbon/glass fiber hybrid ratio and layup angle, and prepared various samples, all of which indicate that carbon/glass hybrid fibers have characteristics such as high strength, large elastic modulus, high stiffness, and light weight compared to glass fiber materials [10–12].

Based on the above, it is feasible to use carbon/glass fiber as a hybrid material as a new type of material for wind turbine blades. However, the new type of carbon/glass hybrid fiber material blades still need to be simulated under various operating conditions and environmental conditions, and the material's stress analysis should be carried out to achieve accurate modeling.

In order to further explore the mechanism of blade vibration, scholars [13,14] studied the natural frequency and natural vibration mode of wind turbine blades, and obtained the changes in blade response and frequency. Ma Jingmin [15] analyzed the free vibration characteristics of the blades, indicating that the natural frequency of the blades is affected by the ply angle, speed, and taper, with the least impact from the speed and the greatest impact from the ply angle. Kan et al. [16] proposed a new predeformation method to compensate blade deformation based on the load increment method, and analyzed the influence of load conditions on blade predeformation by modifying the stiffness matrix. Li Rongrong et al. [17] simplified the wind turbine blades as rotating flexible cantilever beams for dynamic research, and established dynamic differential equations for structural-free vibration based on Hamilton's principle. Zhang et al. [18] used the finite element fluid structure coupling method to study the influence of wind shear on the vibration characteristics of wind turbine blades with geometric nonlinearity. Oh and Yoo [19] used the hypothetical modal method to study the vibration characteristics of pretwisted blades at constant speed under the coupling effects of tension, bending, and torsion. Li Liang et al. [20] simplified the wind turbine blade as a variable cross-section Euler–Bernoulli cantilever beam rotating around the hub for nonlinear flapping analysis.

Wang Zhanyang [21], based on the two-way fluid–structure interaction method, analyzed that the blade deformation is mainly concentrated at the tip, and the blade deformation is mainly waving along the axial direction. When the blades are under different inflow conditions they are mainly subjected to axial forces [22] and the coupled displacement response amplitude gradually increases along the blade span direction, resulting in an increase in inflow velocity and amplitude [23]. Cheng [24] analyzed the composite laminated shell structure of 10 kW wind turbine blades and found that the blade displacement increased with the increase in aerodynamic force, but when the blade reached its maximum speed it was within the safe range. In addition, researchers are committed to exploring fluid–structure interaction vibration of wind turbine blades under different working conditions [25], bending torsional coupling vibration and fault diagnosis [26,27].

The above literature mainly focuses on research methods, ideas, and analysis of blade vibration characteristics. However, the content focuses on the variation patterns of blade displacement and natural frequency, and there is less analysis of blade vibration characteristics based on stress distribution. In this paper, carbon/glass hybrid-fiber reinforced composite laminates were prepared via vacuum assisted resin transfer molding. Their Poisson's ratio and elastic modulus were obtained through experiments, and were imported into the ANSYS software (2022R1) for modeling. Based on the overall dynamic balance equation of the structure, fluid–structure interaction and modal analysis were carried out for the blade, and the blade load distribution and deformation were studied.

At present, carbon fiber material blades and glass fiber material blades have been put into production and use. Carbon fiber materials have excellent performance, and their seismic resistance and deformation resistance are far greater than those of glass fiber wind turbine blades. However, due to the high cost of carbon fiber wind turbine blades, their universality is not strong. In contrast, carbon glass hybrid fiber blades have improved performance and lower cost compared to glass fiber material blades, which is expected to replace traditional blade materials. Therefore, analyzing the vibration characteristics

of carbon glass fiber hybrid blades can help scholars further understand the material and provide further reference for the actual production and use of the blade.

This article produces three different carbon glass hybrid ratio specimens through experiments, measures their mechanical properties, uses Ansys software to model a 10 kW blade, and establishes a flow field for modal analysis and bidirectional fluid structure coupling analysis of the blade. These analysis methods can help engineers evaluate whether the designed structure is reasonable. This article aims to use modal analysis and fluid structure coupling analysis to study the characteristics of the designed blades. Through modal analysis, we can understand the natural frequencies and vibration modes of different blades. The fluid solid coupling analysis investigated the influence of fluid on the modal and deformation of blades with different carbon glass hybrid ratios. Through these analyses, engineers can better understand the performance of carbon glass hybrid blades under actual working conditions.

2. Research Theory

2.1. Sample Tensile Load

The amount of work done by elastic materials during deformation is only related to the initial and current states. Meanwhile, the stress–strain constitutive equation of the laminated plate is

$$[\sigma] = [E][\varepsilon]. \quad (1)$$

In the equation, σ is strength, E is the elastic modulus, and ε is strain.

The tensile stress corresponding to the ultimate load is the tensile strength, and the formula is as follows:

$$F^{tu} = \frac{P^{\max}}{A}. \quad (2)$$

In the equation, F^{tu} is the tensile strength, P^{\max} is the maximum load, and A is the cross-sectional area of the sample.

The formula for elastic modulus is as follows:

$$E = \frac{\Delta\sigma}{\Delta\varepsilon}, \quad (3)$$

$$\nu = -\frac{\Delta\varepsilon_1}{\Delta\varepsilon_2} \quad (4)$$

where E is the elastic modulus, $\Delta\sigma$ is the stress difference, $\Delta\varepsilon$ is the strain difference corresponding to stress difference, $\Delta\varepsilon_1$ is the transverse strain difference, $\Delta\varepsilon_2$ is the longitudinal strain difference, and ν is Poisson's ratio.

2.2. Blade Design Theory

Calculate the diameter of the wind turbine based on its power, using the following formula:

$$P = C_P \frac{\rho}{2} v^3 \eta_1 \eta_2 \frac{\pi D^2}{4}. \quad (5)$$

In the equation, P is output power, ρ is air density, v is the rated wind speed, C_P is the wind energy utilization coefficient, η_1 is the efficiency of wind turbines, η_2 is transmission efficiency, and D is the diameter of the wind turbine.

The is organized as follows:

$$D = \sqrt{\frac{P}{\frac{\rho}{2} \eta_1 \eta_2 C_P \frac{\pi}{4} v^3}}. \quad (6)$$

The formula for calculating the tip speed ratio is

$$\lambda = \frac{n\pi D}{60V}. \quad (7)$$

In the equation, λ is the sharp speed ratio; n is the impeller speed; D is the diameter of the wind turbine; and v is the rated wind speed.

According to Wilson’s theory, optimize the model and calculate parameters such as blade chord length and torsion angle. The mathematical model is as follows:

$$\frac{dC_p}{d\lambda} = \frac{8}{\lambda_0^2} \cdot b(1 - a)F\lambda^3. \tag{8}$$

The constraint formula is

$$b(1 + b)\lambda^2 = a(1 - aF), \tag{9}$$

$$F = \frac{2}{\pi} \arccos(e^{-f}), \tag{10}$$

$$\frac{BcC_L}{r} = \frac{(1 - aF)aF}{(1 - a)^2} \frac{8\pi \sin^2 \varphi}{\cos \varphi}, \tag{11}$$

$$\theta = \varphi - \alpha, \tag{12}$$

$$\text{Re} = \frac{v_0(1 - a)c}{\gamma \sin \varphi}, \tag{13}$$

$$a = \frac{\lambda_0^2}{2000} + 0.027\lambda_0 - 0.038, \tag{14}$$

$$b = \frac{10}{\lambda_0} \cdot e^{\frac{12r}{R}}. \tag{15}$$

In the equation, C_p is the wind energy utilization coefficient; λ_0 is the tip speed ratio; F is the root loss coefficient of the blade; a is the axial induction factor; b is a circumferential inducing factor; φ is installation angle; λ is the speed ratio at different sections of the blade; P is the inflow angle; B is the number of blades; R is the impeller radius; r is the distance from the blade element cross-section to the center of rotation; c is the chord length of the leaf element; C_L is the lift coefficient of the blade airfoil; θ is the torsion angle; α is the best angle of attack; Re is the Reynolds number; and γ is the kinematic viscosity.

2.3. Modal Analysis

The overall dynamic balance equation of a free vibration structure is as follows:

$$[M]\{\ddot{u}\} + [C]\{\dot{u}\} + [K]\{u\} = 0 \tag{16}$$

where $[M]$ is the mass matrix, $\{\ddot{u}\}$ is the node acceleration vector, $[C]$ is the damping matrix, $\{\dot{u}\}$ is the node velocity vector, $[K]$ is the Stiffness matrix, and $\{u\}$ is the node displacement vector.

The modal analysis under the action of no damping or external force can be changed from the above equation as follows:

$$[M]\{\ddot{u}\} + [K]\{u\} = 0. \tag{17}$$

For a linear system:

$$\{u\} = \{\phi\}_i \cos w_i t. \tag{18}$$

In the formula, $\{u\}$ is the vibration mode eigenvector corresponding to the i -th mode, $\{\phi\}_i$ is the natural frequency of the i -th mode, and t is time.

Substituting Equation (7) into Equation (6) yields

$$([K] - [M]w_i^2)\{\phi\}_i = 0 \tag{19}$$

where w_i is the vibration frequency, $\{\phi\}$ is the modal shape, and $[K]$ is the stiffness matrix.

In modal analysis, the size of the stiffness matrix $[K]$ is related to the elastic modulus and Poisson's ratio of the structure, while the size of the mass matrix depends on the density of the structure. Therefore, just knowing the elastic modulus, Poisson's ratio and density of the structure, we can build constant stiffness matrix $[K]$ and mass matrix, and calculate the modal frequency and mode shape of the structure.

3. Blade Material Preparation and Performance Analysis

3.1. Sample Preparation

The reinforcement is a biaxial woven fabric with a ratio of carbon/glass fiber mixed layers of 2:6, 4:4, and 6:2. The biaxial cloth arrangement angles are 0° and 90° , respectively. The woven fabric is composed of warp, weft, and bundled yarn along the thickness direction, which mainly bears the axial load of fiber. The physical image is shown in Figure 1.

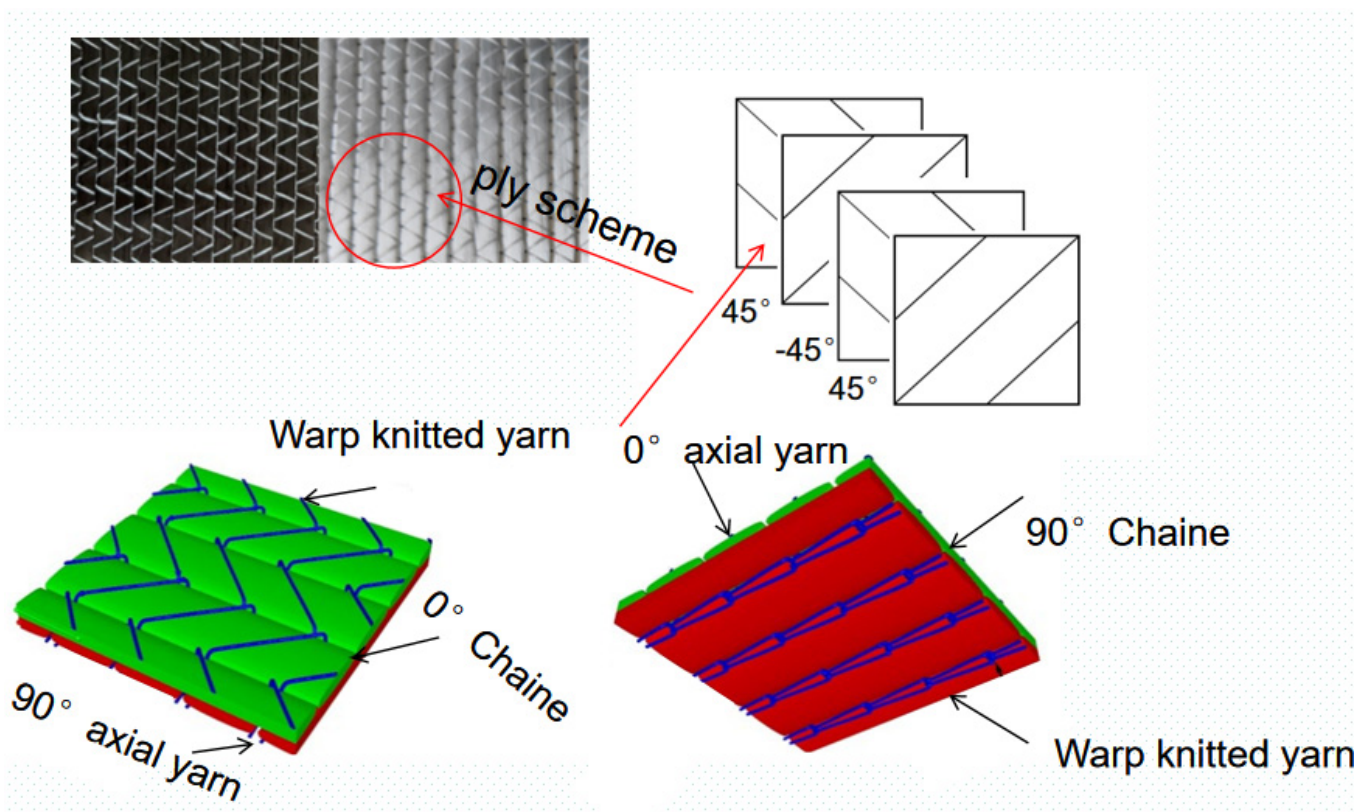


Figure 1. Physical image of biaxial fiber cloth.

This article uses the vacuum-assisted resin transfer molding (VARTM) process to prepare glass-fiber-reinforced composite blade specimens. After the above process, heat the mold, solidify the sheet, and remove the single-layer composite material board from the mold. The sample preparation process is shown in Figure 2.

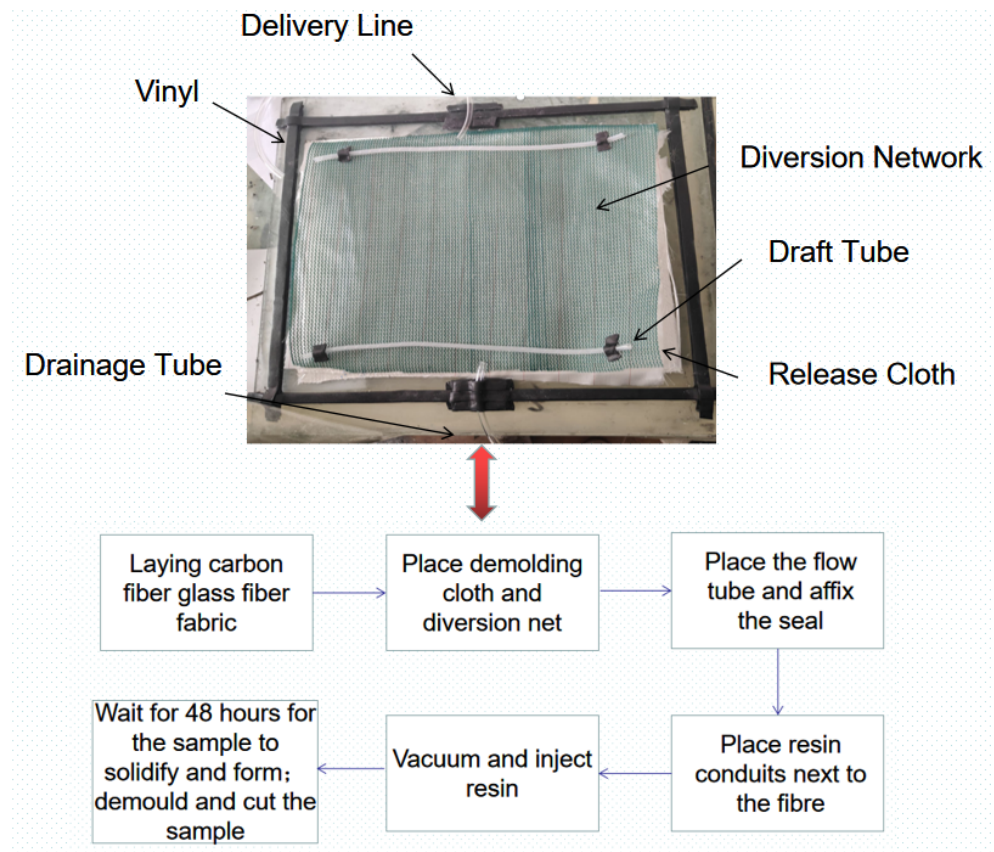


Figure 2. Flow Chart of Composite Material Sample Preparation.

3.2. Material Tensile Performance Testing

Four laminated plates were cut using a CNC cutting machine to prepare corresponding tensile specimens. Five specimens were prepared for each type along the latitude direction. The schematic diagram of the specimens is shown in Figure 3. The sample size requirements are shown in Table 1.

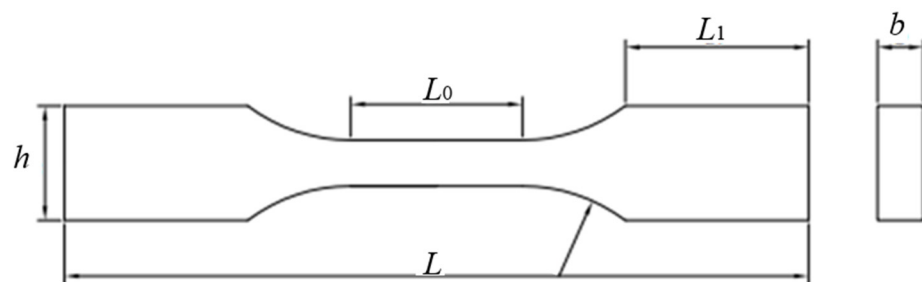


Figure 3. Schematic diagram of tensile specimen.

Table 1. Tensile specimen size parameters.

Symbol	Title	Size/mm
L	Specimen length	250
b	Specimen width	15
h	Specimen thickness	30
L_0	Test length	80
L_1	The length of the piece	50

The spline size parameters are shown in Table 1.

When formulating the experimental design scheme, the calibration pattern of spray paint is utilized to ascertain the dimensions of the tensile test data through DIC speckle deformation analysis. Following the completion of sample production, each type of sample undergoes calibration using the spray painting technique, with the calibration process being finalized by allowing the spray paint to dry. The laboratory is presently equipped with an MTS landmark fatigue testing machine, which is capable of fulfilling the mechanical testing requirements and delivering precise and replicable standard tensile test outcomes. A depiction of the tensile testing procedure for the sample is presented in Figure 4.

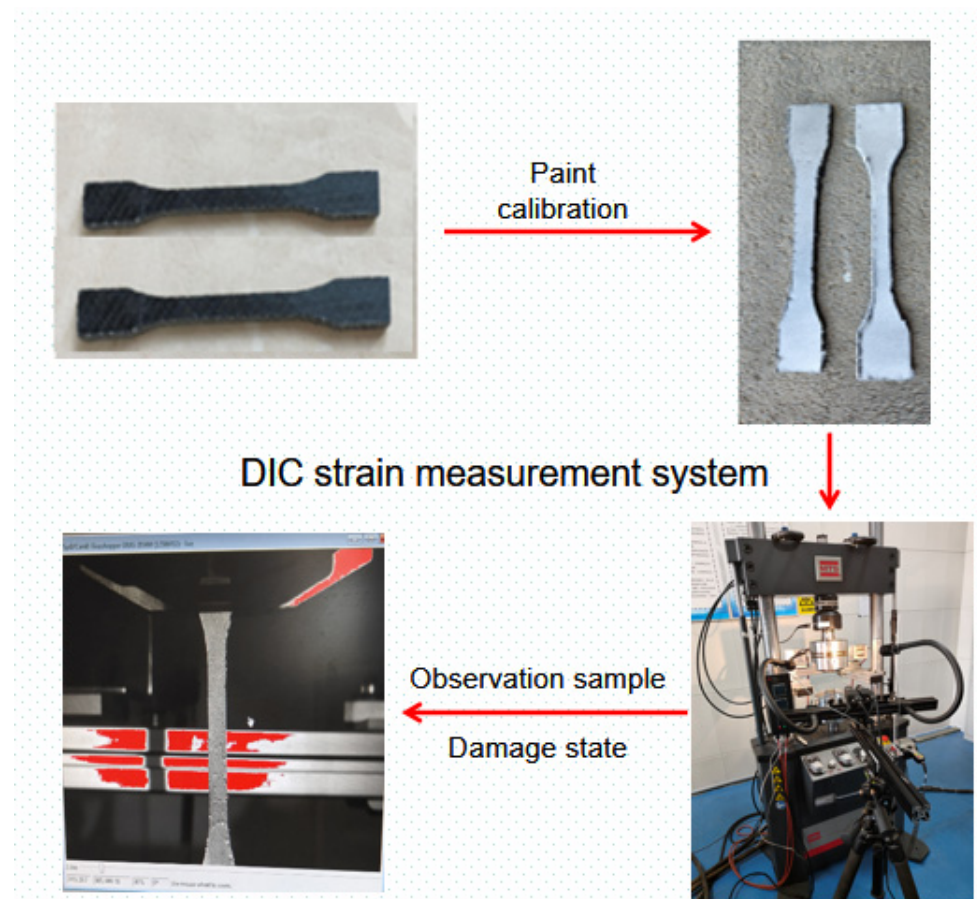


Figure 4. Process of Sample Tensile Testing.

Place the sample vertically on the ground and clamp it with a movement rate of 2 mm/min. Use the WS-3811 digital strain gauge from Shanghai Precision Instruments Co., Ltd. to obtain the load value and displacement variation curve. Figure 5 shows the quasistatic tensile test diagram.

The tensile stress–strain curve of the specimens with different carbon/glass ratios were obtained by breaking the specimens, shown in Figure 6. The performance table of carbon/glass hybrid blade specimens is shown in Table 2.

As shown in Figure 6, the carbon/glass hybrid ratio has a significant impact on the tensile properties of the sample. As the ratio of carbon/glass hybrid layers increases, the tensile stress of the sample increases and the strain decreases. Compared with the glass fiber sample, the sample with a carbon/glass hybrid ratio of 2:6 (cggg) showed a 4.10% increase in stress and a 1.31% decrease in strain. The sample with a carbon/glass hybrid ratio of 4:4 (ccgg) showed a 37.27% increase in stress and a 18.36% decrease in strain. The stress of the specimen (cccg) with a ratio of 6:2 increases by 47.32%, while the strain decreases by 28.36%. This is due to the higher breaking strength and lower elongation at the break of carbon fibers.

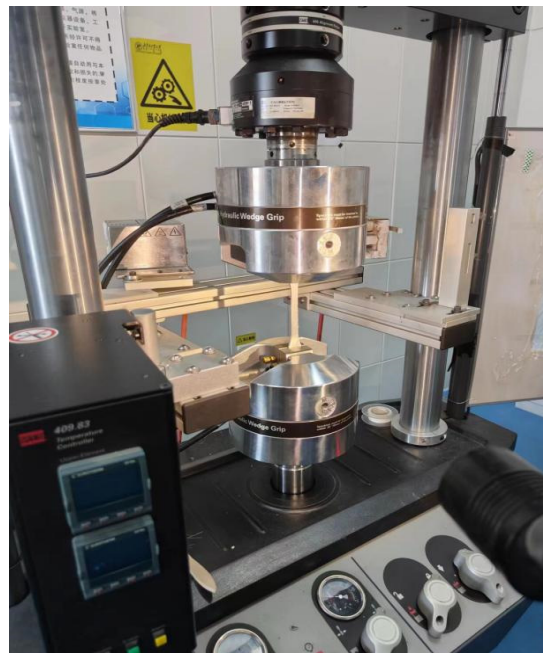


Figure 5. Quasistatic tensile test diagram.

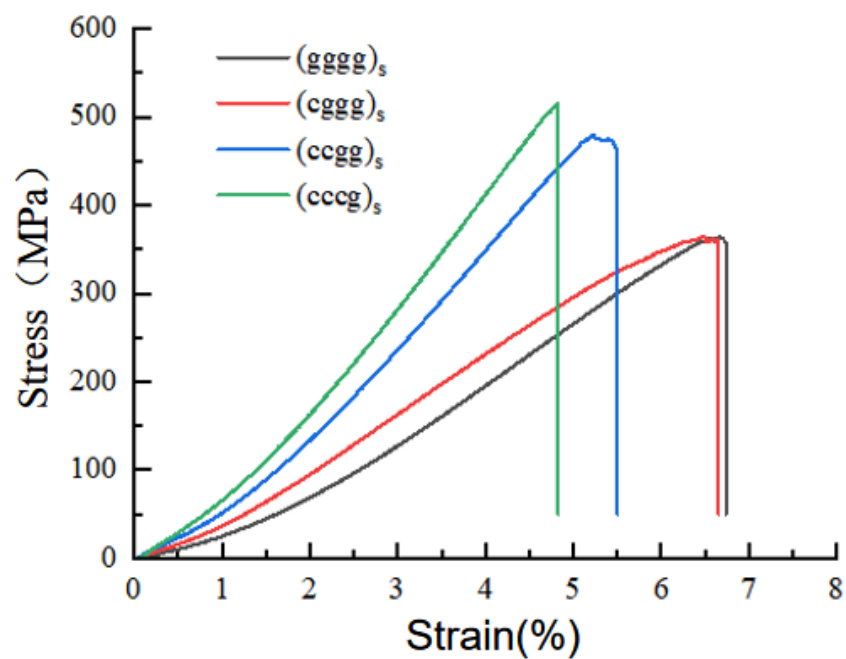


Figure 6. Stress–Strain Curves of Different Carbon/Glass Hybrid Fiber Layer Ratios.

Table 2. Table of Tensile Performance Parameters.

Name	Carbon/Glass Hybrid Ratio	E/(GPa)	G/(GPa)	P/(g·cm ⁻³)
(gggg) _s	0:8	4.72	1.86	1.79
(cggg) _s	2:6	5.15	2.02	1.78
(ccgg) _s	4:4	8.15	3.17	1.73
(cccg) _s	6:2	9.67	3.69	1.73

According to the analysis in the above table, when the carbon/glass hybrid ratio of the sample is 4:4, compared to the hybrid ratio of 2:6, the material properties are significantly

improved, with a relative increase of 34.17% in equivalent strength and 58.27% in equivalent modulus. From this, it can be seen that the carbon to glass ratio shows the greatest trend in performance improvement between 2:6 and 4:4.

4. Numerical Simulation

4.1. Wind Turbine Parameter Design

This article selects the NACA0012 airfoil, with a power of 10 kW and a rated wind speed of 10 m/s, for the design of wind turbine blades.

Determine the blade angle of attack based on the blade lift–drag ratio coefficient, assuming that the blade working environment is between 6 and 14 m/s wind speed, and the fluid Reynolds number range in the flow field is $8.65 \times 10^5 \sim 2.16 \times 10^6$. The lift–drag ratio curve of the NACA0012 airfoil varies with angle of attack as shown in Figure 7:

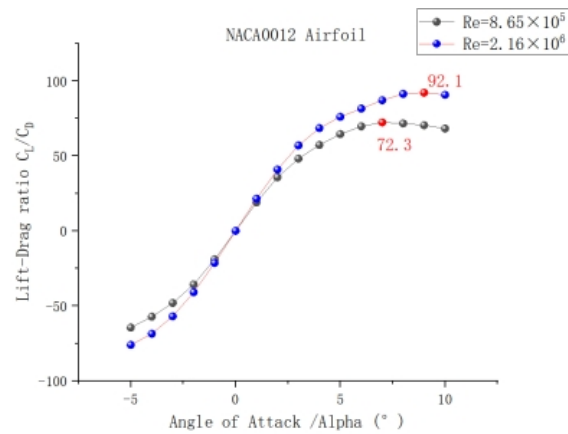


Figure 7. NACA0012 airfoil lift–drag ratio curve.

From the figure, the following can be seen:

When the Reynolds number is $Re = 8.65 \times 10^5$, when the angle of attack is greater than 7° , the lift–drag ratio curve shows a downward trend. The maximum lift-to-drag ratio is 72.3, and the angle of attack is 7° . At an attack angle of 8° , the decrease in lift–drag ratio is not significant.

When the Reynolds number is $Re = 2.16 \times 10^6$, when the angle of attack is greater than 9° , the lift–drag ratio curve shows a downward trend. The maximum lift-to-drag ratio is 92.1, and the angle of attack is 9° . At an attack angle of 8° , the rise in lift–drag ratio is not significant.

Take the median Reynolds number of 1.5×10^6 as a reference. The change curves of lift coefficient and drag coefficient obtained are shown in Figure 8, and the detailed data are shown in Table 3.

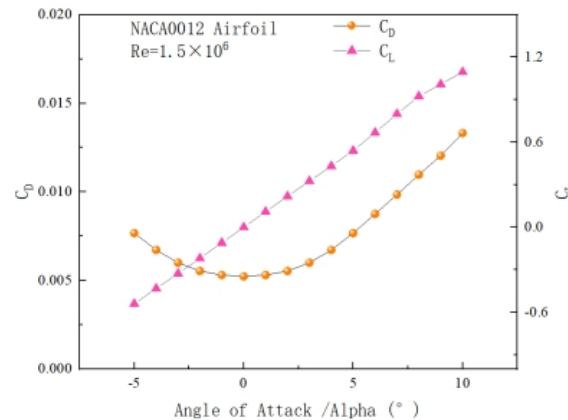


Figure 8. Curve of lift–drag coefficient changing with angle of attack.

Table 3. Section airfoil parameter table.

NACA0012 Airfoil, $Re = 1.5 \times 10^6$				
$\alpha / ^\circ$	C_L	C_D	C_L / C_D	C_M
−5	−0.5404	0.00767	−70.456	−0.0052
−4	−0.4317	0.00672	−64.241	−0.0044
−3	−0.3263	0.006	−54.383	−0.0027
−2	−0.2187	0.00553	−39.547	−0.0016
−1	−0.1097	0.0053	−20.698	−0.0007
0	0	0.00523	0	0
1	0.1098	0.0053	20.716	0.0007
2	0.2188	0.00553	39.566	0.0015
3	0.3263	0.006	54.383	0.0027
4	0.4317	0.00672	64.241	0.0044
5	0.5404	0.00767	70.456	0.0052
6	0.6677	0.00875	76.308	0.0015
7	0.8002	0.00984	81.321	−0.0034
8	0.924	0.01097	84.229	−0.0067
9	1.0088	0.01204	83.787	−0.0016
10	1.0958	0.01332	82.267	0.0028

From the table, it can be seen that the lift–drag ratio is the highest at an angle of attack of 8° , with a maximum value of $C_L / C_D = 84.229$, a lift coefficient of 0.924, and a drag coefficient of 0.01097. In summary, the attack angle of wind turbine blades should be selected as 8° in the current environment.

The rated speed n of a 10 kW small wind turbine is 160 rad/min, and the diameter of the wind turbine is calculated to be 10 m, resulting in a tip–speed ratio of approximately 7.

Using MATLAB, perform iterative calculations on a and b , assigning the initial values of a and b to 0. With the above formula, the modified chord length c and torsion angle θ can be calculated. The blade length is 4.8 m, and it is divided into 10 segments for design. The calculation results are shown in Table 4.

Table 4. Section Airfoil Parameters Table.

Section	Chord Length	Torsional Angle	a	b
0.1R	0.698	22.57	0.323831	0.350373
0.2R	0.609	10.21	0.335469	0.106903
0.3R	0.475	3.74	0.336935	0.049591
0.4R	0.379	−0.04	0.337211	0.028315
0.5R	0.312	−2.48	0.337791	0.018288
0.6R	0.264	−4.17	0.339174	0.012825
0.7R	0.229	−5.43	0.342193	0.009572
0.8R	0.202	−7.42	0.34914	0.007571
0.9R	0.178	−7.30	0.367484	0.0065
1.0R	0.133	−8.39	0.432106	0.007097

4.2. Wind Turbine Model Establishment and Laying

This article uses ANSYS software to model a blade with an airfoil of NACA0012 and a power of 10 kW. The shell extraction entity is shown in Figure 9.

Establish a grid division model for the sector blade periodic symmetric impeller model. The entire model adopts tetrahedral surface grid division, using global settings, and selecting tetrahedral and triangular grid types for the free surface grid. The number of model nodes obtained is 79,849 and the total number of units is 79,886. The grid quality is evaluated using the unit quality coefficient, which provides a comprehensive quality measurement standard ranging from 0 to 1. The closer the value is to 1 the better the grid quality. After inspection, the average grid quality of the model is 0.82834, which can ensure the normal operation of subsequent solving steps.

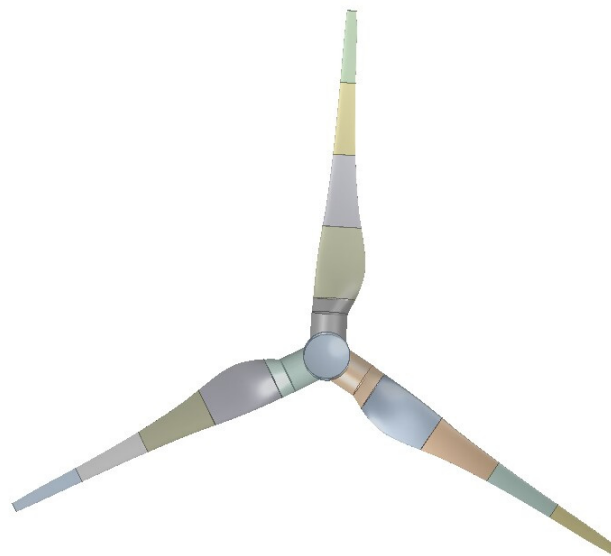


Figure 9. 10 kW Wind Turbine Blade Model.

Enter 3 properties of carbon/glass hybrid materials, divide the blades into 5 parts, and establish new laying rules for each part as shown in Table 5.

Table 5. Lamination Methods of Composite Material Blades.

Area (m)	0~0.8	0.8~1.8	1.8~2.8	2.8~3.8	3.8~4.8
Layers	8	7	6	5	4

Set the fiber thickness of each layer to 2.9 mm, and set the laying direction along the blade span to 0°. The blade after laying is shown in Figure 10.

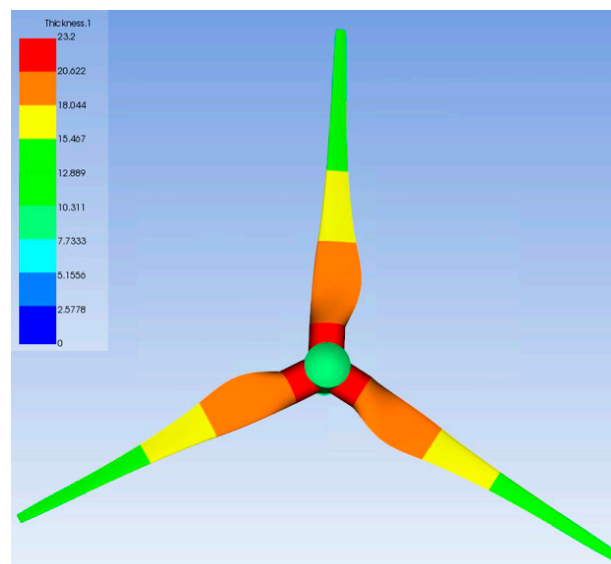


Figure 10. Blade Layer Model.

4.3. Flow Field Setting and Coupling Treatment

Establish a flow field domain based on blade size, with a flow field domain size of 10 m × 10 m × 30 m, with CFD preference and Fluent solver. By using tetrahedral and triangular meshes, a total of 2,929,461 nodes and 1,031,559 elements were obtained. Divide the grid as shown in Figure 11.

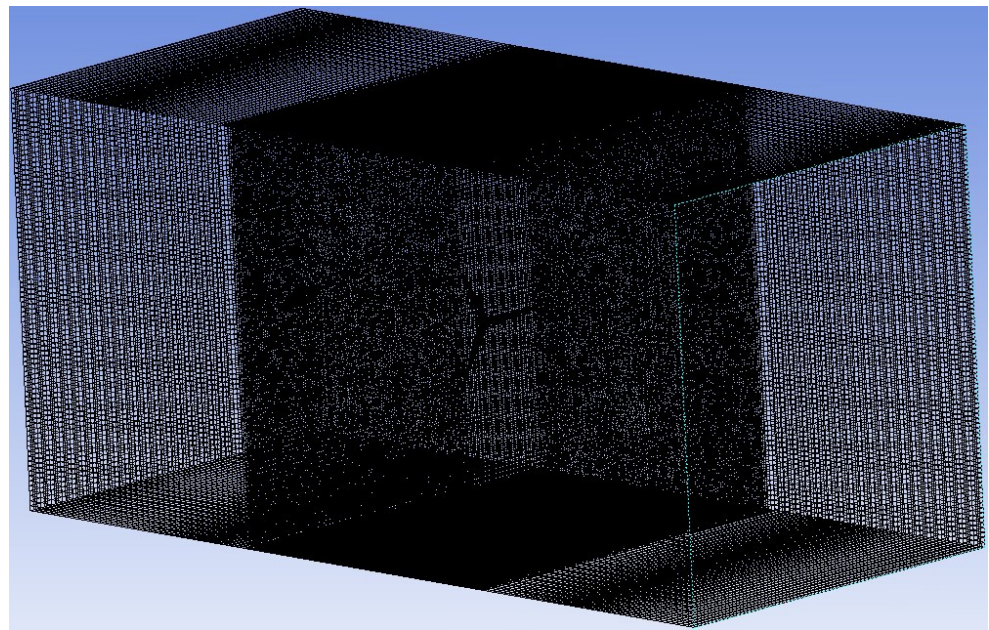


Figure 11. Flow Field Domain Grid Division.

Set the fluid velocity inlet section and average static pressure outlet section in CFD, with a fluid inlet velocity of 10 m/s. Set the entire blade and flow field boundary as a fluid solid coupling surface. The minimum length of the dynamic grid is 0.0082, the maximum length is 0.56, and the twist degree does not exceed 0.9. After coupling the Fluent module with the ACP (pre) module and achieving stability, the pressure cloud map of the fluid on the entity is obtained as shown in Figure 12.

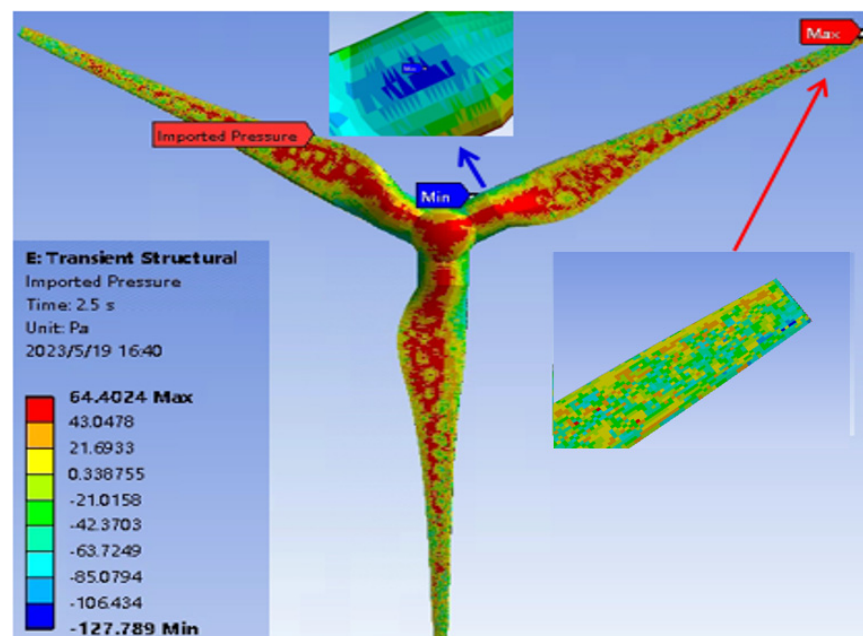


Figure 12. Blade surface pressure distribution diagram.

According to the figure, the maximum positive pressure value on the blade surface is 64.4024 Pa, distributed in the middle section of the blade. The maximum negative pressure of the blade is -127.789 Pa, mainly distributed at the root of the blade. Set the hub surface as the constraint surface, rotate the entire blade around the Y-axis at the rated speed of

160 rad/min, set the entire blade as the fluid–structure interaction surface, set the time step as 0.01 s, and calculate and solve the blade.

The entire simulation process is shown in Figure 13:

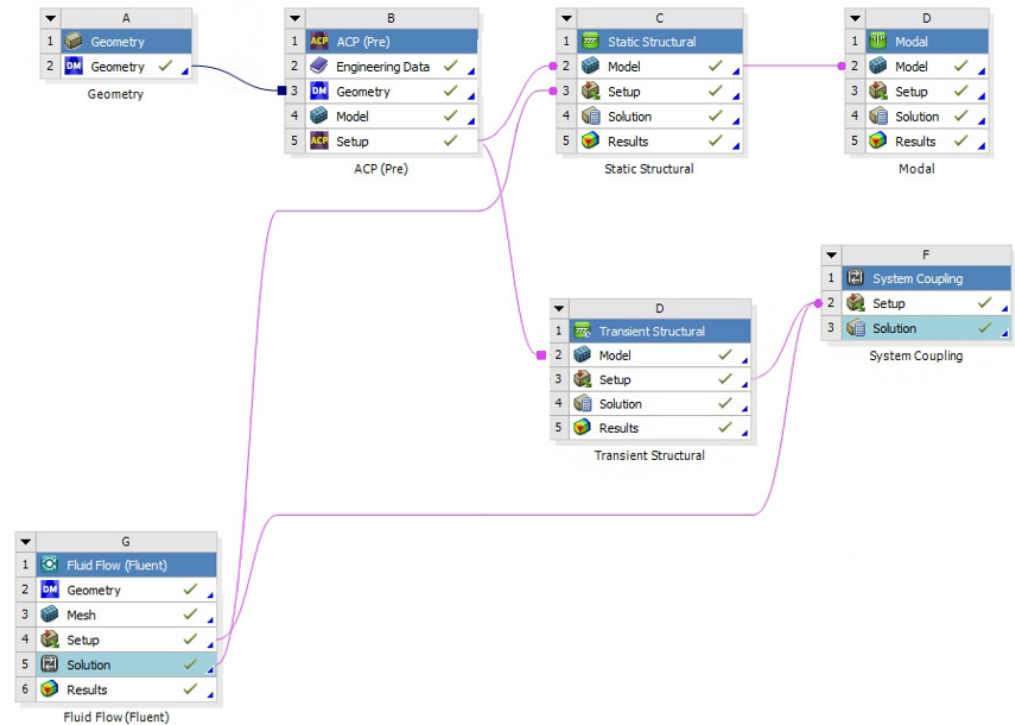


Figure 13. Blade simulation process.

4.4. Grid Independence Verification

To ensure accurate structural field calculations of the wind turbine model, we adopted a multiregion grid partitioning method. By dividing the wind turbine model into multiple regions, details in the structural field can be better captured. At the same time, in order to improve the accuracy of the calculation, we have encrypted the grid to make it more dense. This can better simulate the structural characteristics of the wind turbine and ensure the accuracy of the calculation results. Figure 14 shows the division of the wind turbine structural field model.

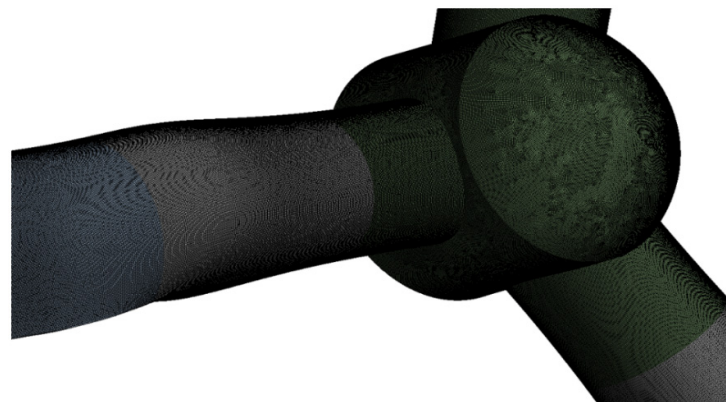


Figure 14. Grid division of structural field.

To verify the grid independence in the structural field, we conducted calculations under rated wind speed of 10 m/s and rated speed of 160 r/min. We used different numbers of structural field grids to calculate the equivalent stress and deformation of the blades. The validation results are shown in Table 6:

Table 6. The validation results.

Number of Grids	62,541	67,536	72,589	79,886	86,852
Maximum equivalent stress/MPa	41.2	41.8	42.5	43.2	43.2
Maximum deformation/m	0.036	0.038	0.042	0.044	0.044

From Table 6, it can be seen that as the number of structural field grids increases, the values of equivalent stress and deformation gradually tends to stabilize. When the number of grids reaches 79,886, the values of equivalent stress and deformation basically do not change significantly. Therefore, we can conclude that for this specific working condition, using 79,886 structural field grids can obtain more accurate results, and further mesh refinement has little impact on the calculation results.

5. Analysis of Blade Vibration Characteristics

5.1. Deformation Displacement Analysis

Name the blades of three different hybrid materials, as shown in the Table 7 below:

Table 7. Blade Specimens with Carbon/Glass Hybrid Ratios.

Name	(c/g)Hybrid Ratio
A ₁	2:6
A ₂	4:4
A ₃	6:2

If the influence of blade deformation on the flow field is not taken into account, the performance of three composite material blades with different carbon/glass hybrid ratios will be compared, the influence of flow velocity on the magnitude of blade deformation under different working conditions will be calculated, and the velocity deformation curve will be fitted. The variation in deformation of three materials with flow velocity is shown in Figure 15.

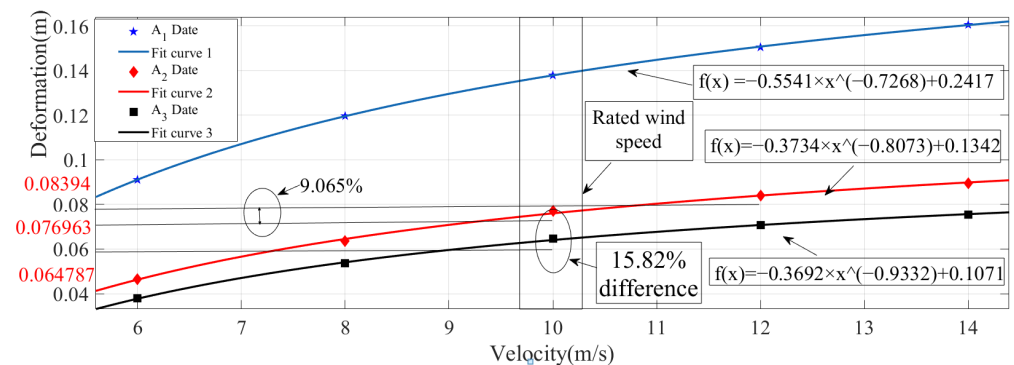


Figure 15. Trend Chart of Blade Deformation under Different Materials.

From Figure 11, it can be seen that the deformation degree of A1 is much greater than that of A2 and A3, while the deformation of A2 and A3 is relatively small. When the flow velocity is within 6–10 m/s, the deformation trend of the three types of blades is relatively large, which is due to the wind force acting on the blades, which to some extent causes protrusion deformation. As the wind speed increases, the force of the flow field on the blades increases, and the deformation of the blades gradually increases. When the flow velocity is 10–14 m/s, the deformation trend of the blade decreases with the increase in the flow rate. This may be due to the increase in bending stiffness when the blade deforms to a certain extent, offsetting some of the stress. Afterwards, the deformation of the blade

gradually stabilizes, possibly due to a slight depression, which causes the deformation of the blade to first increase and then decrease. When the flow rate reaches the rated flow rate in the flow field, the A2 shape variable is 0.07696 m and the A3 shape variable is 0.06479 m. Compared with A1, the deformation resistance of A2 and A3 is significantly improved, and the difference in deformation between A2 and A3 is 15.82%. The improvement in deformation resistance is relatively small. At a flow rate of 12 m/s, the A2 shape variable is 0.08394 m. Due to the increase in bending stiffness, the blade deformation only increases by 9.065%.

5.2. Modal Analysis

In the undamped and prestressed state, the root of the blade is constrained and the three blade modes have the same vibration mode. The first six modal frequencies of the blade are shown in Table 8, and the first six modal modes of the blade are shown in Figure 16:

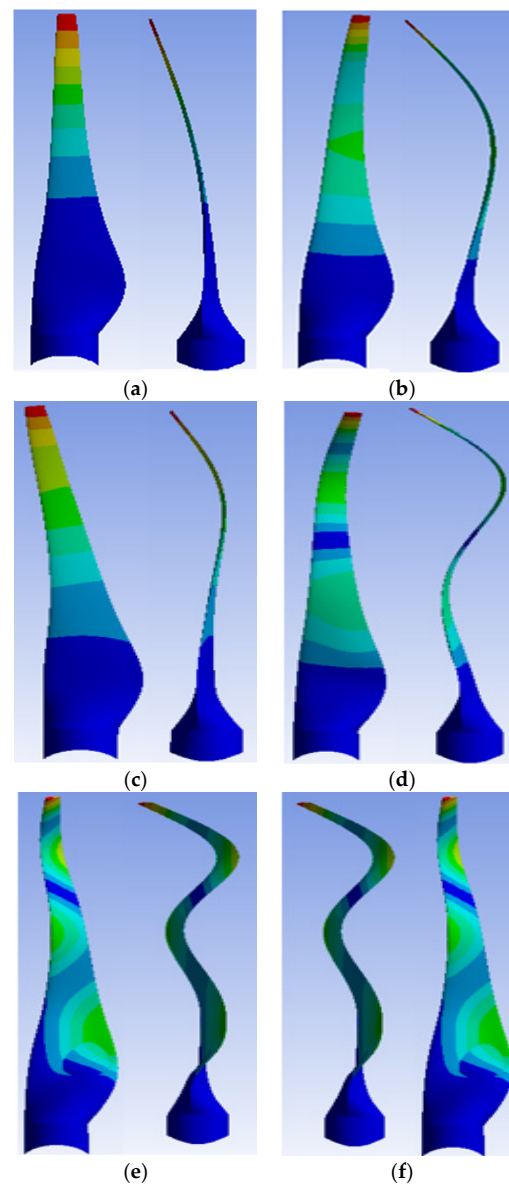


Figure 16. Blade First–Six Order Modal Map. (a) First-order swing. (b) Second-order swing and oscillation. (c) Third-order swing+oscillation. (d) Fourth-order swing+oscillation+torsion. (e) Fifth-order swing+swing+twist. (f) Sixth-order swing+swing+twist.

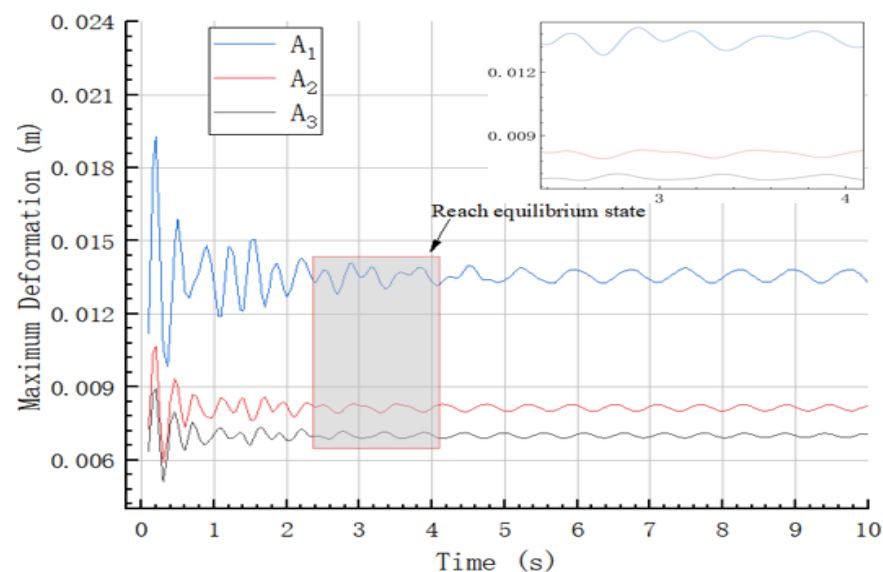
Table 8. Numerical Table of Blade Modal Frequencies.

Mode	A ₁ /(Hz)	A ₂ /(Hz)	A ₃ /(Hz)
1	1.1622	1.5567	1.6993
2	4.1850	5.6070	6.1202
3	7.3824	9.8382	10.7360
4	8.8847	11.7420	12.8360
5	10.9560	14.3170	15.6960
6	13.5870	17.9140	19.6110

From the table, it can be seen that compared to A₁, the first- to sixth-order modal frequencies of A₂ differ by 0.3945 Hz, 1.4220 Hz, 2.4558 Hz, 2.8573 Hz, 3.3610 Hz, and 4.3270 Hz, respectively. The vibration frequencies of each order vary greatly, indicating that the carbon–glass ratio between 2:6 and 4:4 has a significant impact on the blade modal frequencies. Compared to A₂, A₃ has a frequency difference of 0.1426 Hz, 0.5132 Hz, 0.8978 Hz, 1.0940 Hz, 1.3790 Hz, and 1.6960 Hz in the first- to sixth-order modes. It can be seen that the carbon to glass ratio between 4:4 and 6:2 has a relatively small impact on the modal frequency of the blade as the carbon content continues to increase.

5.3. Vibration Characteristic Analysis

Three types of blades were introduced into the transient structural wind field. Due to the maximum shape variation in the leading edge vertex of the airfoil at the blade tip, the displacement time variation curves in the X, Y, and Z directions were monitored, and the data were fitted to obtain the displacement time variation diagrams of the three types of blades, as shown in Figures 17–19.

**Figure 17.** Maximum Displacement Curve of Blade in X-Direction.

From the above figure, it can be seen that the curve tends to converge without divergence, and the displacement of the monitoring points gradually decreases and stabilizes in all directions. A₁ takes longer to reach equilibrium compared to A₂ and A₃. From the X and Y directions, the equilibrium time for A₂ and A₃ is 3 s and the equilibrium time for A₁ is 5 s. From the Z direction, the equilibrium time for A₂ and A₃ is 2.5 s, and the equilibrium time for A₁ is 4 s.

The total deformation of A₂ and A₃ intensifies during the first 3 s, and then shows periodic changes over time. A₁ was affected by deformation in three directions in the first 4 s, resulting in an increase in total deformation. During the period of 4 to 5 s, the Z

direction showed periodic changes, while the X and Y directions remained unstable. After 5 s, the total deformation also showed periodic changes over time.

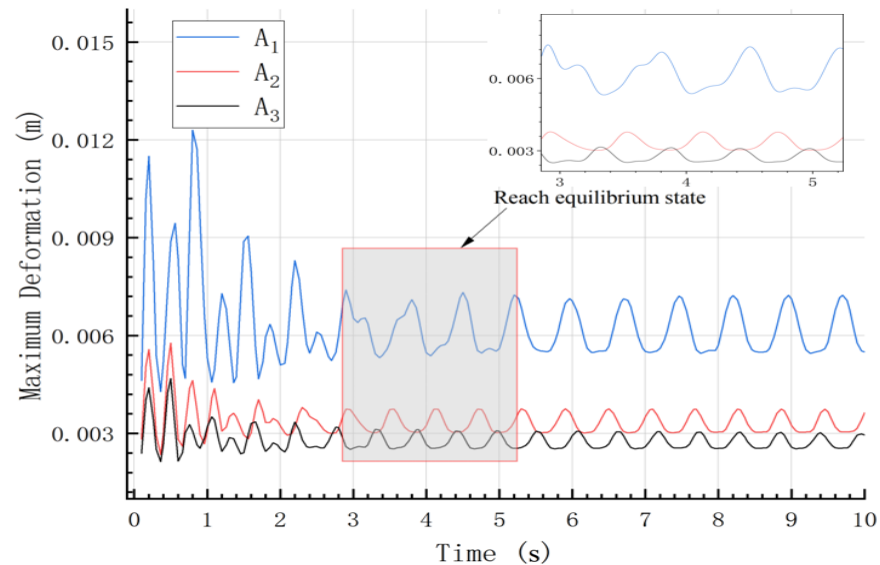


Figure 18. Maximum Displacement Curve of Blade in Y-Direction.

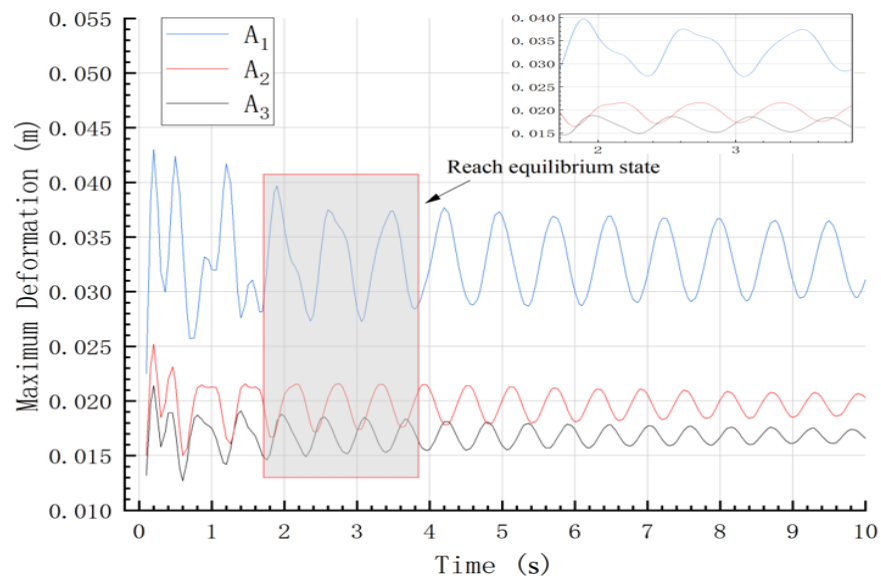


Figure 19. Maximum Displacement Curve of Blade in Z-Direction.

Due to blade deformation being determined by three directions, the first cycle of vibration for A1, A2, and A3 blades is 0.3007 s, 0.2745 s, and 0.2584 s. The second cycle is 0.3492 s, 0.3020 s, and 0.3005 s. The third cycle is 0.3001 s, 0.2515 s, and 0.2330 s. The first cycle is 3.3260 Hz, 3.6430 Hz, and 3.8700 Hz. The second cycle is 2.8637 Hz, 3.3113 Hz, and 3.3278 Hz. The third cycle is 3.3320 Hz, 3.9760 Hz, and 4.2916 Hz. From the above data, it can be seen that under the action of a 10 m/s wind field, the vibration frequencies of the three types of blades are all higher than their corresponding first order frequency and lower than their corresponding second order frequency. However, the vibration frequency of A1 is similar to its second order natural frequency, so the amplitude difference between A1, A2, and A3 is relatively significant. From the figure, it can be seen that the deformation of the blades in the Z direction is large, and the deformation degree in the X and Y directions is relatively small. The performance of A2 and A3 is significantly better than that of A1, but the performance improvement between A2 and A3 is not significant.

The vibration modes of the three types of blades are similar, and the main vibration form of the blades is waving. In order to better understand the deformation process of the blades, it is necessary to conduct stress analysis on the surface of the blades. Due to the symmetry of the wind turbine blades, take A3 blades with good performance for analysis, as shown in Figure 20.

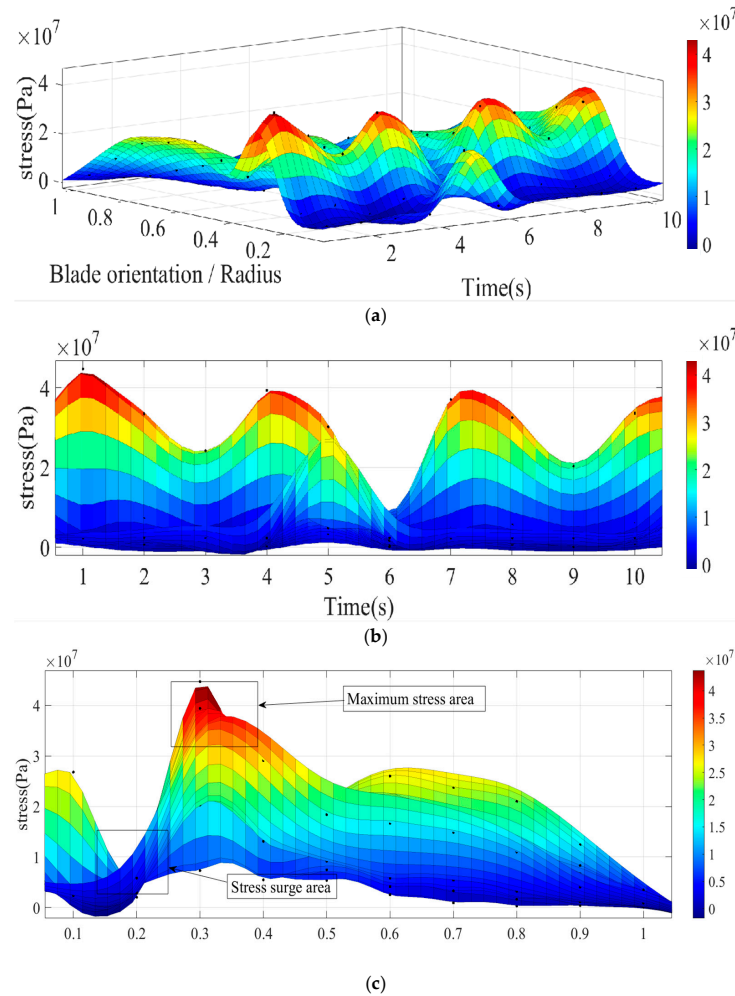


Figure 20. Blade Stress Distribution Diagram. (a) Three dimensional diagram of blade stress distribution. (b) Blade stress changes over time. (c) Blade stress changes with spanwise direction.

From the above figure, it can be seen from the spanwise axis that the stress on the blade is mainly concentrated along the 1/3 of the spanwise direction of the blade. This is due to the interaction between air and the blade, which exerts a force on the blade, resulting in stress and deformation of the blade. These deformations and stress distributions will in turn affect the flow state of air, thereby altering the characteristics of fluid motion. From the time axis, the stress on the blades is the smallest at 3 s, 6 s, and 9 s, and the stress on the blades is the lowest at $t = 5$ s. This may be due to the deformation of the blades and changes in the direction of fluid velocity.

6. Conclusions

Laminated plates and blade reinforcements have similar structures. In this paper, a new type of carbon/glass fiber hybrid material is used as the blade reinforcement. Different carbon glass hybrid materials are selected and laminated plates are prepared using an epoxy resin matrix. Based on the material constitutive equation and modal analysis theory, the tensile properties of the materials are analyzed, and a 10 kW NACA0012 blade model is established. Three types of blade vibration modes, displacement changes, and stress

distributions with a carbon/glass fiber hybrid ratio of 2:6, 4:4, and 6:2 are discussed. The following conclusions are drawn:

- (1) Under the same process and layer angle, the tensile performance of blades with a carbon/glass hybrid ratio of 4:4 was significantly improved compared to 2:6. Subsequently, as the carbon content of the sample increased the improvement in blade performance became smaller. Therefore, it is estimated that the maximum improvement in tensile performance was achieved between 6:2 and 4:4 for the blades.
- (2) As the wind speed in the flow field increases the maximum deformation of the blade gradually increases, and the improvement in deformation resistance of blade A1 to blade A2 is most significant. From the velocity deformation fitting curve, compared to blade A1, the deformation trend of A2 and A3 blades is more stable, and the overall deformation resistance is better.
- (3) From modal analysis and the maximum displacement curve under rated wind speed, it can be seen that the displacement changes in all three directions of the blades tend to converge, and the vibration frequency is greater than its corresponding first-order fixed frequency and less than its second-order fixed frequency, without resonance phenomenon. The main vibration form of the blades is waving. Blade A2 and blade A3 reach equilibrium after 3 s, while A1 takes 5 s to reach equilibrium.
- (4) From the stress distribution diagram, it can be seen that the concentrated force on the blade is at 1/3 of the position and exhibits periodic changes. This change may lead to the deformation of the blade, causing changes in the flow field structure near the blade and the phenomenon of blade waving.

Author Contributions: Conceptualization, X.J. and Y.J.; Methodology, X.J. and X.G.; Software, Y.J. and K.Z.; Validation, Y.J., M.G. and J.S.; Formal analysis, L.F. and S.W.; Investigation, J.S.; Resources, X.J. and Y.J.; Data curation, X.J. and Y.J.; Writing—original draft, Y.J.; Writing—review & editing, Y.J.; Supervision, X.J.; Project administration, X.J. and X.G.; Funding acquisition, X.J. and X.G. All authors have read and agreed to the published version of the manuscript.

Funding: The research of this project has won the general project of the National Natural Science Foundation of China (approval number: 12272189), Supported By Program for Young Talents of Science and Technology in Universities of Inner Mongolia Autonomous Region (approval number: NJYT23022), the Research Science Institute of colleges and universities in Inner Mongolia—key project (approval number: NJZZ22395), the basic research business fund project of colleges and universities directly under the Inner Mongolia (approval number: JY20220119), and the Research Science Institute of Inner Mongolia University of Technology—doctoral fund (approval number: BS2021056).

Informed Consent Statement: All authors have read and agree to the published version of the manuscript.

Data Availability Statement: Data cannot be shared openly but are available on request from authors. Except for the data provided in the article, other data is our specialized research and therefore cannot be shared.

Conflicts of Interest: The authors declare no conflict of interest.

References

1. Li, L.; Li, M.; Jin, F. The Application of Vibration Detection Technology in Fault Monitoring of Wind Turbine Blade Cracks. *Therm. Power Eng.* **2013**, *28*, 207–212.
2. Navadeh, N.; Goroshko, I.; Zhuk, Y.; Etmnan Moghadam, F.; Soleiman Fallah, A. Finite element analysis of wind turbine blade vibrations. *Vibration* **2021**, *4*, 310–322. [[CrossRef](#)]
3. Awadallah, M.; El Sinawi, A. Effect and detection of cracks on small wind turbine blade vibration using special Kriging analysis of spectral shifts. *Measurement* **2020**, *151*, 107076. [[CrossRef](#)]
4. Xu, Z.; Anyu, L. Fluid–structure interaction analysis of composite blade of wind turbine. *J. Shenyang Univ. Technol.* **2019**, *2*, 138–142.
5. Bosheng, H.; Hecai, S.; Yaping, P. Study on the hybrid effect and mechanical properties of carbon/glass hybrid fibers. *High Tech. Fibers Appl.* **2005**, *30*, 39–41.
6. Gao, X.P.; Tao, N.N.; Yang, X.R.; Wang, C.; Xu, F.J. Quasi static three point bonding and facade behavior of 3-D orthogonal woven composites. *Compos. B. Eng.* **2019**, *159*, 173–183. [[CrossRef](#)]

7. Gao, X.P.; Wang, C.; Wu, W.; Li, Y.G. Improvement on facade performance of 3-D orthogonal woven composite with nanoclay modification. *Fibers Polym.* **2021**, *10*, 1–8.
8. Gao, D.; Zhang, Y.; Fang, D.; Ding, C.; Yan, H.; Ji, D. Compressive property analysis and strength versus slenderness ratio relationship prediction for carbon/glass hybrid fiber reinforced polymer bars. *Constr. Build. Mater.* **2022**, *317*, 125955. [[CrossRef](#)]
9. Shuai, Z.; Jia, Z.-Y.; Bo, H.O.U. Tensile properties of unidirectional carbon fiber-glass fiber hybrid reinforced epoxy composites in layer. *Acta Mater. Compos. Sin.* **2016**, *33*, 297–303.
10. Liu, J.; Qi, R.; Cao, Q. Study on mechanical properties and failure mechanism of carbon/glass hybrid fiber composites. *New Chem. Mater.* **2022**, *50*, 153–157.
11. Fu, L.; Jiang, X.; Sun, Z.; Wen, S.; Gao, M.; Tian, R. The Effect of Carbon/Glass Hybrid Fiber Layered Structure on the Bending and Torsional Coupling Characteristics of Wind Turbine Blades. *J. Compos. Mater.* **2022**, *40*, 1–9.
12. Yang, R.; Liu, Y.; Wang, G.; Wu, Z. Tensile properties of multi-directional glass carbon fiber hybrid composites. *Synth. Resin Plast.* **2018**, *35*, 78–82.
13. Bin, Z.; Yuting, L.; Jingyu, W. Random vibration analysis of large wind turbine blades. *J. Gansu Sci.* **2019**, *31*, 64–69.
14. Lijun, S.; Jingyuan, L. Analysis of Vibration Characteristics of 3 MW Wind Turbine Blades. *Renew. Energy* **2019**, *37*, 1067–1072.
15. Jingmin, M.; Yongsheng, R. Analysis of Free Vibration Characteristics of Wind Turbine Blades. *Vib. Shock.* **2015**, *34*, 105–110.
16. Kan, D.; Wang, Y.L.; Zhong, J.J.; Liu, Z.H. Pre Transformation Method for Manufactured Compressor Blade Based on Load Incremental Approach. *Int. J. Turbojet Engines* **2020**, *37*, 259–265.
17. Rongrong, L.; Zhongmin, W.; Xiaosha, Y. The vibration characteristics of a rotating FGM circular ring shaped flexible beam. *J. Appl. Mech.* **2017**, *34*, 417–423.
18. Zhang, J.; Guo, L.; Wu, H.; Zhou, A.; Hu, D.; Ren, J. The impact of wind shear on vibration of geometrically nonlinear wind turbine blade under fluid—Structureinteraction. *Ocean. Eng.* **2014**, *84*, 14–19. [[CrossRef](#)]
19. Oh, Y.; Yoo, H.H. Vibration analysis of a rotating pre twisted blade considering the coupling effects of stretching, bonding, and torsion. *J. Sound Vib.* **2018**, *431*, 20–39. [[CrossRef](#)]
20. Liang, L.; Yinghui, L.; Qikuan, L. Nonlinear Wave Analysis of Wind Turbine Blades. *J. Solid Mech.* **2012**, *33*, 98–102.
21. Wang, Z.; Zhang, L.; He, L.; Wang, J.; Hu, Y. Analysis of output power of horizontal axis wind turbine based on bidirectional Fluid—structure interaction. *J. Drain. Irrig. Mach. Eng.* **2017**, *35*, 975–980.
22. Li, D.; Ying, Z. Study on the Influence of Inlet Flow Conditions on the Fluid-Solid Coupling Characteristics of Wind Turbine Blades. *Hydraul. Pneum. Seal.* **2022**, *42*, 17–24.
23. Chen, Y. A Study on the Coupling of Wind Turbine Blade Load, Displacement, and Stress/Strain. Ph.D. Thesis, Inner Mongolia University of Technology, Hohhot, China, 2017.
24. Cheng, T.H.; Oh, I.K. *Fluid Structure Coupled Analyses of Composite Wind Turbine Blades*; Advanced Materials Research Trans Tech Publications Ltd.: London, UK, 2007; Volume 26, pp. 41–44.
25. Bofeng, X.; Zixuan, Z.; Chengjun, D.; Xin, C.; Tongguang, W.; Zhenzhou, Z. The effect of wind shear on the aerodynamic performance and wake shape of wind turbine blades. *J. Mech.* **2021**, *53*, 362–372.
26. Zifei, X.; Minnan, Y.; Chun, L. Analysis and diagnosis of chaotic space fault of wind turbine bearing based on Convolutional neural network. *Therm. Power Eng.* **2020**, *35*, 243–250+256.
27. Hao, W. Research on the Vibration Characteristics of Wind Turbine Blades under High Wind Speed. Ph.D. Thesis, Anhui University of Science and Technology, Huainan, China, 2019.

Disclaimer/Publisher’s Note: The statements, opinions and data contained in all publications are solely those of the individual author(s) and contributor(s) and not of MDPI and/or the editor(s). MDPI and/or the editor(s) disclaim responsibility for any injury to people or property resulting from any ideas, methods, instructions or products referred to in the content.